APL Materials

Atomic layer epitaxy of kagome magnet Fe_3Sn_2 and Sn-modulated heterostructures

Cite as: APL Mater. **10**, 061112 (2022); https://doi.org/10.1063/5.0094257
Submitted: 01 April 2022 • Accepted: 31 May 2022 • Published Online: 24 June 2022

Shuyu Cheng, Binbin Wang, Igor Lyalin, et al.

Atomic layer epitaxy of kagome magnet Fe_3Sn_2 and Sn-modulated heterostructures

Cite as: APL Mater. 10, 061112 (2022); doi: 10.1063/5.0094257
Submitted: 1 April 2022 • Accepted: 31 May 2022 •
Published Online: 24 June 2022

Shuyu Cheng,[1] Binbin Wang,[2] Igor Lyalin,[1] Núria Bagués,[2] Alexander J. Bishop,[1] David W. McComb,[2,a)] and Roland K. Kawakami[1,b)]

AFFILIATIONS

[1] Department of Physics, The Ohio State University, Columbus, Ohio 43210, USA
[2] Department of Materials Science and Engineering, The Ohio State University, Columbus, Ohio 43210, USA

Note: This paper is part of the Special Topic on Materials Challenges and Synthesis Science of Emerging Quantum Materials.
[a)]**Electronic mail:** mccomb.29@osu.edu
[b)]**Author to whom correspondence should be addressed:** kawakami.15@osu.edu

ABSTRACT

Magnetic materials with kagome crystal structure exhibit rich physics, such as frustrated magnetism, skyrmion formation, topological flat bands, and Dirac/Weyl points. Until recently, most studies on kagome magnets have been performed on bulk crystals or polycrystalline films. Here, we report the atomic layer molecular beam epitaxy synthesis of high-quality thin films of topological kagome magnet Fe_3Sn_2. The structural and magnetic characterization of Fe_3Sn_2 on epitaxial Pt(111) identifies highly ordered films with c-plane orientation and an in-plane magnetic easy axis. Studies on the local magnetic structure by anomalous Nernst effect imaging reveal in-plane oriented micrometer size domains. Superlattice structures consisting of Fe_3Sn_2 and Fe_3Sn are also synthesized by atomic layer molecular beam epitaxy, demonstrating the ability to modulate the sample structure at the atomic level. The realization of high-quality films by atomic layer molecular beam epitaxy opens the door to explore the rich physics of this system and investigate novel spintronic phenomena by interfacing Fe_3Sn_2 with other materials.

In recent years, studies on magnetic topological materials with kagome lattices have become one of the hottest frontiers of condensed matter research, owing to their exotic physical properties in both real space and momentum space.[1,2] In momentum space, angle-resolved photoemission spectroscopy (ARPES) experiments on Mn_3Sn, Fe_3Sn_2, FeSn, and CoSn[3–6] show that kagome lattices give rise to Dirac cones and flat bands that are topologically protected and are of particular interest. In addition, scanning tunneling spectroscopy finds evidence for topological flat bands as a sharp peak in the local density of states.[7] These topologically nontrivial features result in signatures of anomalous transport (e.g., chiral anomaly) in magnetotransport experiments.[3,8] Furthermore, it is theoretically predicted that the band structures of the kagome topological magnets can be controlled by tuning their magnetic structures.[1,3] In real space, the kagome topological magnets have layered structures with spins occupying corner-sharing triangular lattices, which leads to geometrical spin frustration.[9,10] A surprisingly large anomalous Hall effect (AHE) and magneto-optic Kerr effect (MOKE) have been reported in noncollinear antiferromagnet Mn_3Sn, even with vanishingly small net magnetization.[10,11] Skyrmion spin textures have been observed in ferromagnetic Fe_3Sn_2 resulting from the competition of exchange, dipolar, and Zeeman energies.[12,13] However, most of the studies on the kagome magnets have been done on bulk materials[4,5,9–15] with a few papers reporting the growth and characterization of epitaxial films.[16–20] Looking forward, the heterostructures consisting of kagome magnets will be interesting for both fundamental research and applications, owing to the possibility of tuning the magnetic and topological properties via interface interactions, epitaxial strain, and quantum confinement. However, all the reported studies on epitaxial Fe_3Sn_2 thin films have been focusing on high temperature growth so far, which may not allow for the formation of well-defined heterostructures due to

interdiffusion at elevated temperatures. Therefore, lower temperature growth of Fe_3Sn_2 is desired for the future development of heterostructures and superlattices based on kagome magnets.

In this paper, we report the atomic layer molecular beam epitaxy (AL-MBE) growth of high-quality Fe_3Sn_2 thin films on $Pt(111)/Al_2O_3(0001)$ substrates at lower temperatures. By sequentially depositing Fe_3Sn kagome layers and Sn_2 layers [see Fig. 1(a)], we can control the sample structure at the atomic level. The crystalline structure of our Fe_3Sn_2 sample is confirmed by a combination of *in situ* reflection high energy electron diffraction (RHEED), x-ray diffraction (XRD), and transmission electron microscopy (TEM). Energy-dispersive x-ray spectroscopy (EDX) shows sharp interfaces for low temperature growth. The magnetic properties of Fe_3Sn_2 are investigated by using MOKE, superconducting quantum interference device (SQUID), and anomalous Nernst effect (ANE). Using a microscopy technique based on ANE, we successfully image the in-plane oriented domain structure of the epitaxial Fe_3Sn_2 films and investigate the magnetization reversal as a function of the applied field. We further utilize AL-MBE to precisely control the stacking sequences of Fe_3Sn and Sn_2 atomic layers, making superlattices with modulation of Sn_2 layers, and confirm their structures by TEM and EDX. This demonstrates the potential of using AL-MBE to generate designer materials consisting of kagome layers (Mn_3Sn, Fe_3Sn, Co_3Sn, etc.) and Sn_2 spacer layers with precision control of sample structures at the atomic level.

Fe_3Sn_2 is a ferromagnet with a high Curie temperature, T_C = 670 K[21], and saturation magnetization of 1.9 μ_B per Fe at low temperature.[4] Figure 1(a) shows the crystal structure of Fe_3Sn_2 (space group R$\bar{3}$m, with lattice constants a = 5.338 Å and c = 19.789 Å[21]), which consists of Fe_3Sn kagome layers and Sn_2 spacer layers. In each Fe_3Sn monolayer, the Fe atoms form corner-sharing equilateral triangles surrounding hexagons, with Sn atoms sitting in the center of the hexagons. The alternating sequence of one Sn_2 monolayer with honeycomb lattice and two Fe_3Sn kagome layers produces the layered crystal structure of Fe_3Sn_2.

Based on this layered structure, we synthesized Fe_3Sn_2 thin films on top of epitaxial Pt(111) buffer layers on $Al_2O_3(0001)$ substrates by AL-MBE. The epitaxial growth was performed in an MBE chamber with a base pressure of 4×10^{-10} Torr. Films were deposited on $Al_2O_3(0001)$ substrates (MTI Corporation) prepared by annealing in air at 1000 °C for 3 h followed by annealing in ultrahigh vacuum (UHV) at 500 °C for 30 min. A 5 nm Pt(111) buffer layer was deposited from an e-beam evaporator (Pt: 99.99%, Kurt J. Lesker) onto the Al_2O_3 (0001) substrate by growing the first 0.6 nm at 440 °C and the rest 4.4 nm while cooling down from 140 to 80 °C. The Pt buffer layer was post-annealed at 300 °C to improve the crystallinity and surface roughness. The Fe_3Sn_2 layer was grown on Pt(111) at 100 °C by using the following AL-MBE sequence: deposit two atomic layers of Fe_3Sn with a Fe:Sn flux ratio of 3:1, deposit one atomic layer of Sn_2 with the growth time same as two Fe_3Sn layers, and then repeat. The Fe and Sn fluxes were generated from Knudsen cells (Fe: 99.99%, Alfa Aesar; Sn: 99.998%, Alfa Aesar), and the growth rates were determined by using a quartz deposition monitor that was calibrated by x-ray reflectometry. Typical growth rates were ~0.85 Å/min, ~0.67 Å/min, and ~0.45 Å/min for Fe, Sn, and Pt, respectively. To protect the sample from oxidation, a 5 nm CaF_2 capping layer was deposited on top of the Fe_3Sn_2.

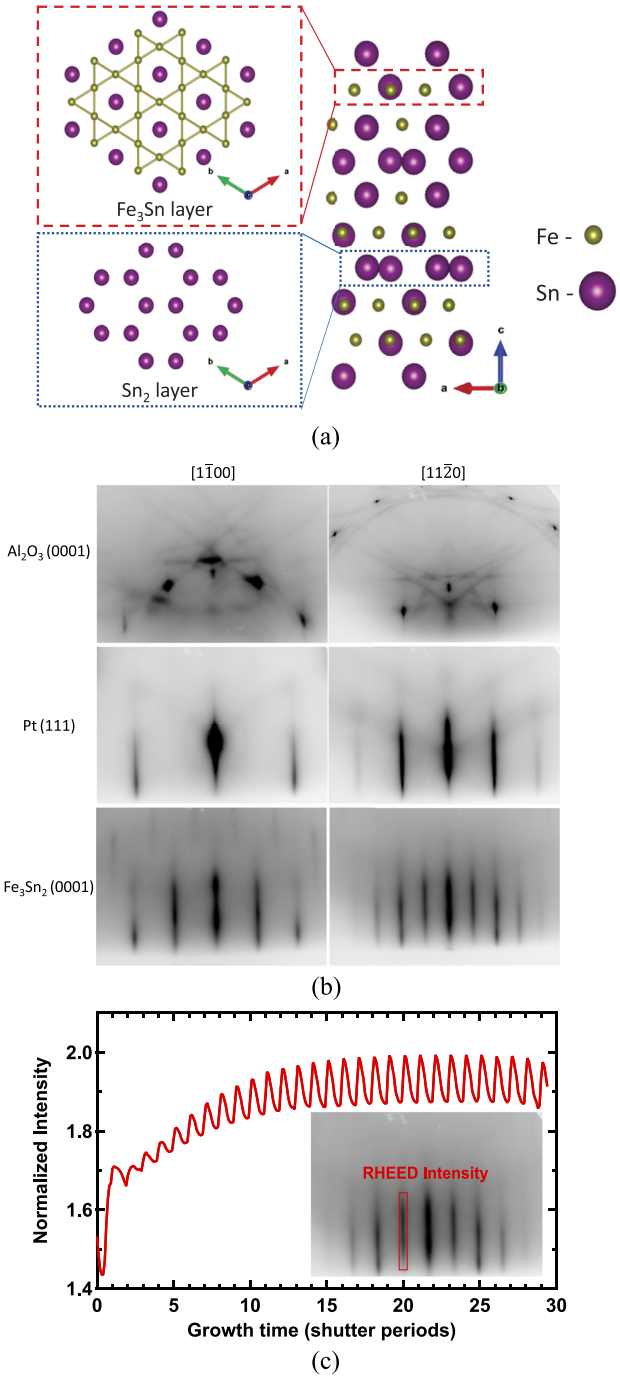

FIG. 1. Material structure and growth. (a) Left: Top view of an individual Fe_3Sn layer with kagome structure (top) and Sn_2 layer with honeycomb structure (bottom). Right: Side view of the crystal structure of Fe_3Sn_2 consisting of alternating stacking of two Fe_3Sn kagome layers and one Sn_2 layer. (b) RHEED patterns for the $Al_2O_3(0001)$ substrate, 5 nm Pt film, and 20 nm Fe_3Sn_2 film measured with the beam along [1$\bar{1}$00] (left column) and [11$\bar{2}$0] (right column) directions of the substrate. (c) Oscillations in the normalized RHEED intensity as a function of time. The RHEED intensity is measured within the red box and normalized by the intensity of the whole image as background.

RHEED patterns were measured during growth to characterize the epitaxial growth and determine the in-plane lattice constants. Figure 1(b) shows the RHEED patterns for the $Al_2O_3(0001)$ substrate (top row), the 5 nm Pt buffer layer (middle row), and the Fe_3Sn_2 layer after 20 nm of growth (bottom row). The left and right columns show the patterns taken for the beam along the $[1\bar{1}00]$ and $[11\bar{2}0]$ directions of the substrate, respectively. With in-plane rotation of the sample, RHEED exhibits the same pattern every 60° (i.e., sixfold rotation symmetry) with the patterns alternating between $[1\bar{1}00]$-type and $[11\bar{2}0]$-type every 30°. For the in-plane epitaxial alignment, the Pt(111) and $Fe_3Sn_2(0001)$ surface unit cells are aligned with each other and rotated 30° with respect to the $Al_2O_3(0001)$ substrate, as $a_{Al_2O_3} \approx (\sqrt{3}/2)2a_{Pt} \approx (\sqrt{3}/2)a_{Fe_3Sn_2}$ (bulk values for in-plane lattice constant are $a_{Al_2O_3}$ = 4.759 Å, $2a_{Pt}$ = 5.549 Å, and $a_{Fe_3Sn_2}$ = 5.338 Å).

The streaky patterns observed during Fe_3Sn_2 growth signify diffraction from a two-dimensional surface. In addition, we observe oscillations [Fig. 1(c)] in the normalized RHEED intensity where the maxima occurs for the Fe_3Sn termination and the minima occurs for the Sn_2 termination. The normalization is performed by dividing the intensity of the background and is helpful for canceling variations in the incident beam intensity and background lighting. Except for the change in the RHEED intensity, we did not observe any other significant difference in the RHEED patterns between Sn_2 and Fe_3Sn terminations. Nevertheless, the presence of the RHEED oscillations in atomic layer MBE confirms the modulation of the surface termination during growth.

Films grown by this method were studied with XRD using the Cu Kα line (wavelength 1.5406 Å) to analyze their crystal structure. A representative 2θ-ω scan of a 20 nm film grown at 100 °C is shown in Fig. 2(a) and includes the Fe_3Sn_2 (0009) peak with several Laue oscillations, indicating a smooth film. The out-of-plane lattice parameter extracted from the analysis of this scan is 19.85 Å, which agrees well with previous reports of 19.789 Å.[21] A peak from the 5 nm Pt(111) buffer also shows the Laue oscillations with larger angular period due to smaller thickness of the Pt layer in

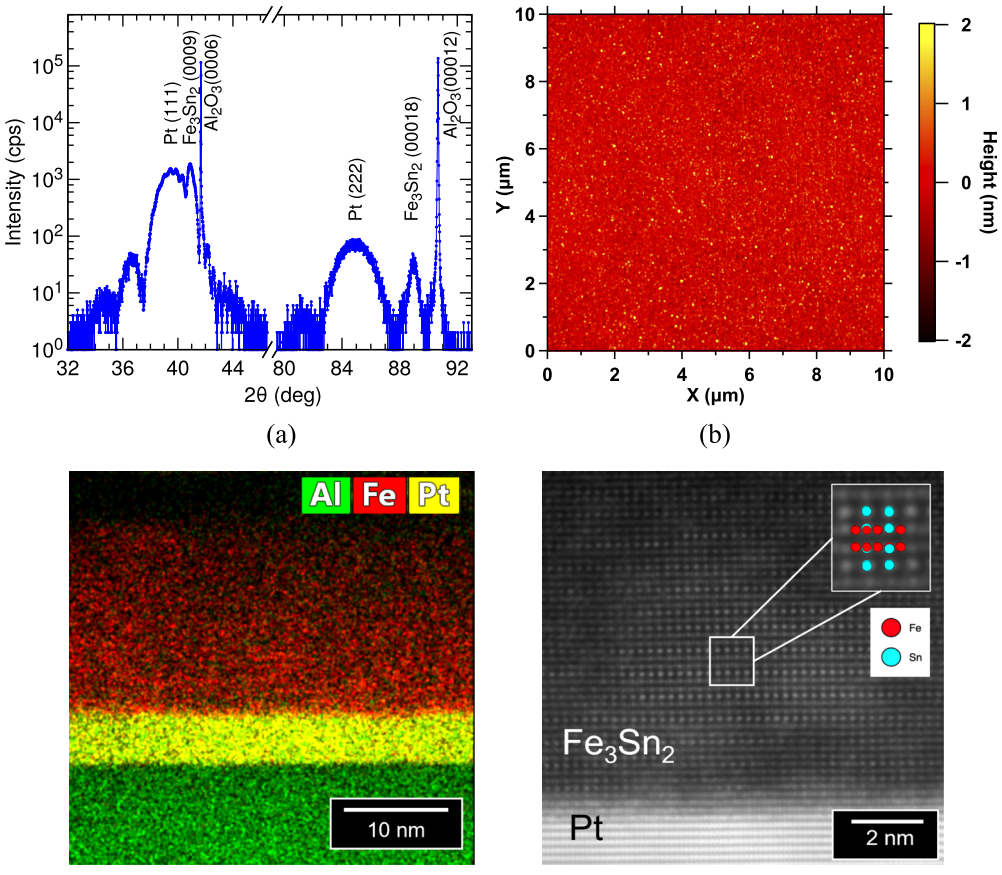

FIG. 2. Material characterization. (a) 2θ-ω scan of a 20 nm Fe_3Sn_2 film grown on c-sapphire. (b) AFM scan over a 10 × 10 μm^2 area on the surface of a 20 nm Fe_3Sn_2 film (rms roughness 0.362 nm). (c) Cross-sectional EDX-STEM chemical map of a 20 nm Fe_3Sn_2 sample grown at 100 °C. (d) Atomic resolution HAADF-STEM imaging of a 20 nm Fe_3Sn_2 sample grown at 100 °C viewed along the Fe_3Sn_2 $[11\bar{2}0]$ direction. The upper right insert is magnified from the white box and overlaps the projected unit cell of Fe3Sn2 along Fe_3Sn_2 $[11\bar{2}0]$ direction.

comparison with Fe_3Sn_2 layer (Pt Laue peaks at ~34.5°, ~36.7°, and ~43.5°), demonstrating the high quality of the buffer layer. At larger 2θ angles, we observe Fe_3Sn_2 (00018) and Pt(222) peaks, with no additional peaks that could be attributed to the impurity phases (see the supplementary material, Sec. 2, for full range scans and rocking curve data).

To characterize the surface topography of the sample, we performed atomic force microscope (AFM) measurements on uncapped 20 nm Fe_3Sn_2 films. Figure 2(b) shows a typical 10 × 10 μm^2 scan of a 20 nm Fe_3Sn_2 sample grown at 100 °C. The AFM image indicates that the sample has a flat surface, with a root-mean-square (rms) roughness of 0.362 nm.

An important factor for material synthesis is the growth temperature. To optimize the growth temperature, we performed AFM and XRD measurements on a series of samples grown at different temperatures ranging from room temperature to 200 °C. The AFM and XRD results are shown in the supplementary material, Secs. 1 and 2, respectively. We conclude that 100 °C is the optimized growth temperature as it gives the best AFM roughness and sharp XRD peaks.

The epitaxial quality of the 20 nm Fe_3Sn_2 sample grown at 100 °C was examined by using a probe-corrected Themis Z S/TEM at 200 kV. Figures 2(c) and 2(d) show the energy-dispersive x-ray (EDX) chemical map and cross-sectional scanning transmission electron microscopy (STEM) image, revealing a clear interface between the Pt buffer and Fe_3Sn_2 thin film. The stoichiometry of Fe_3Sn_2 thin films was confirmed by electron energy loss spectroscopy (EELS), which gives an atomic ratio of Fe:Sn ≈ 1.5 (see the supplementary material, Sec. 3, for details). To identify the crystalline quality of the Fe_3Sn_2 thin films, atomic resolution high-angle annular dark-field (HAADF) STEM images of the Fe_3Sn_2/Pt interface were acquired along the Fe_3Sn_2 [$11\bar{2}0$] direction [see Fig. 2(d)]. Since the contrast in HAADF STEM is approximately proportional to the square of the atomic number, the Sn atoms in the Sn_2 atomic layers appear as the brightest spots, while the atoms in Fe_3Sn kagome layers are dimmer (the atomic numbers of Sn and Fe are 50 and 26, respectively). The alternating sequence of one Sn_2 monolayer and two Fe_3Sn kagome layers shows a highly crystalline film with the expected Fe_3Sn_2 phase, although some stacking faults are observed.

To investigate the in-plane and out-of-plane magnetic properties of the Fe_3Sn_2 films, we measured the longitudinal and polar MOKE hysteresis loops. The samples were probed using a linearly polarized He–Ne laser (633 nm wavelength, ~100 μW power, and ~100 μm spot size) and a polarizing beamsplitter, photodiode bridge, and lock-in amplifier (463 Hz intensity modulation) to detect the Kerr rotation. The laser beam had a ~45° angle of incidence for longitudinal MOKE and normal incidence for polar MOKE. Figure 3(a) shows a representative longitudinal hysteresis loop (red curve) measured on a 20 nm thick Fe_3Sn_2 sample. The square hysteresis loop with a coercivity of 2.4 mT indicates ferromagnetic order with in-plane magnetization. In contrast, the polar hysteresis loop (blue curve) shows a small Kerr rotation with slight variation with the out-of-plane magnetic field. Together, the longitudinal and polar MOKE loops show that the Fe_3Sn_2 samples have an easy-plane magnetic anisotropy. This agrees with previous studies of Fe_3Sn_2 films grown by sputter deposition[19] and in bulk crystals thinned to below ~100 nm.[22] In addition, Fe_3Sn_2 thin films have very weak magnetic anisotropy within the sample plane, which is shown by our longitudinal MOKE data as a function of different in-plane directions (see the supplementary material, Sec. 4).

We also performed SQUID magnetometry measurements on our Fe_3Sn_2 films (see the supplementary material, Sec. 5, for SQUID measurement details). Figure 3(b) shows hysteresis loops of a 20 nm thick Fe_3Sn_2 sample measured with in-plane (red curve) and out-of-plane (blue curve) magnetic fields. The in-plane hysteresis loop exhibits a sharp switching behavior, while the out-of-plane hysteresis loop exhibits almost linear behavior within ±1 T and saturates at ~1 T, suggesting that our Fe_3Sn_2 samples have easy-plane anisotropy. Furthermore, our SQUID results give a saturation magnetization M_s = 1.9 μ_B/Fe (630 kA/m), which is consistent with previous studies.[14,19]

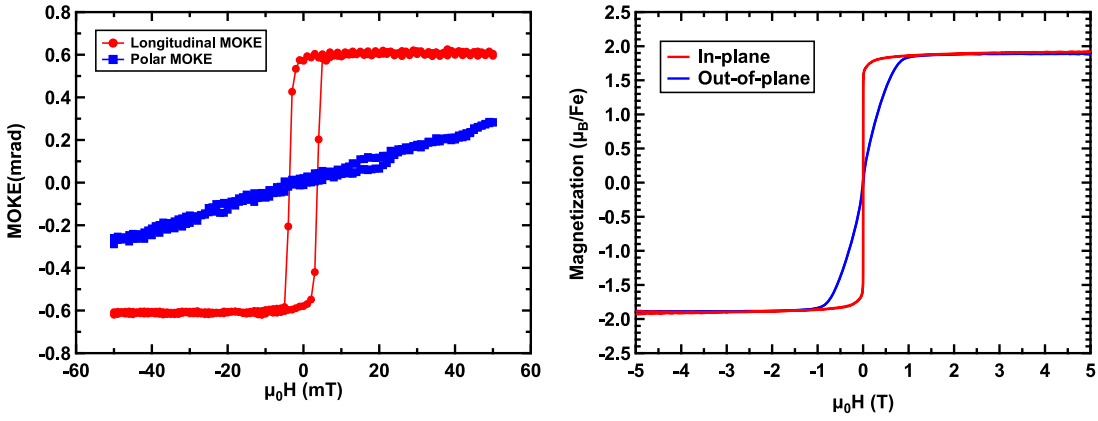

(a) (b)

FIG. 3. Magnetic properties of Fe_3Sn_2 films. (a) Longitudinal (red) and polar (blue) MOKE hysteresis loops of a 20 nm Fe_3Sn_2 film. (b) Magnetic hysteresis loops of a 20 nm Fe_3Sn_2 film measured using SQUID magnetometry with in-plane (red) and out-of-plane (blue) geometries.

The magnetic domain structures of Fe_3Sn_2 films are of interest due to the observation of skyrmions in bulk Fe_3Sn_2, but have not yet been studied in thin films. Longitudinal MOKE microscopy with oblique angle incidence can detect the in-plane magnetization and, therefore, determine the in-plane domain structure of our Fe_3Sn_2 films. However, in this paper, we choose to use thermal gradient microscopy (TGM)[23–25] over longitudinal MOKE to image the domain structure because we found that it has a better signal-to-noise ratio in our experimental setup.

TGM is based on moving a laser spot over the sample surface and recording a voltage induced by the local laser heating. The thermal gradient generated in the out-of-plane direction Z and a component of magnetization in the X direction give rise to the anomalous Nernst effect, which is detected as a voltage along the Y direction, $V_{ANE} \sim [\nabla T \times \mathbf{M}]$ [see Fig. 4(a)].

For the ANE imaging, we fabricated 10 μm wide Hall bar devices by a combination of photolithography and argon ion milling [Fig. 4(b)]. The laser excitation for the thermal gradient was produced by a frequency-doubled (BaB_2O_4 crystal) mode-locked Ti:sapphire laser for a wavelength of 400 nm. The laser beam with 0.7 mW power was focused by a 50× objective lens (NA of 0.6) to a spot size of 0.9 μm, and a fast steering mirror in the 4f alignment scheme was used for scanning the laser spot over the sample surface. The intensity of the beam was modulated at a frequency of 120 kHz and the generated ANE voltage was detected using a lock-in amplifier.

We first utilized the ANE microscope to measure a detailed hysteresis loop at a fixed position. As shown in Fig. 4(c) for the magnetic field along the X direction, the hysteresis loop shows a gradual reversal followed by magnetization switching with a coercivity of 2.3 mT. This has a similar coercivity but more gradual initial reversal than the in-plane hysteresis loops obtained by MOKE [Fig. 3(a)]. The origin of the different hysteresis properties is revealed by imaging the magnetic domain structure of Fe_3Sn_2 films at a series of magnetic fields. A representative sequence during the magnetization reversal is shown in Fig. 4(d). Starting at −10.0 mT, the magnetization is in a saturated state along $-X$ (blue). The reversal initiates with the nucleation of white regions with $M_x \approx 0$, mainly at the edges of the sample. This can be explained by the minimization of domain wall energy as the edge boundary does not contribute a domain wall energy cost. The nucleation at the edges initiates magnetization reversal, which results in a more rounded hysteresis loop compared to the uniform films. With increasing magnetic field, the domains of opposite polarity grow inward and coalesce across the channel. At about +1.5 mT, the magnetic structure is in a multidomain state with characteristic features (e.g., blue and red regions) ranging from 1 to 10 μm in size. By +2.5 mT, most of the magnetic moments have switched to $+X$ direction, with only a few regions remaining along $-X$. Finally, at +10.0 mT, the magnetization reversal is complete and the films are fully saturated along $+X$.

Finally, to demonstrate the ability to control the sample structure at the atomic level, we synthesized a [Fe_3Sn_2 (2 nm)/Fe_3Sn (2 nm)]$_5$ superlattice using the AL-MBE technique. The [Fe_3Sn_2/Fe_3Sn]$_5$ superlattice samples were grown under the same conditions as Fe_3Sn_2 samples but with different atomic layer deposition sequences. For a 2 nm Fe_3Sn layer, we deposit nine

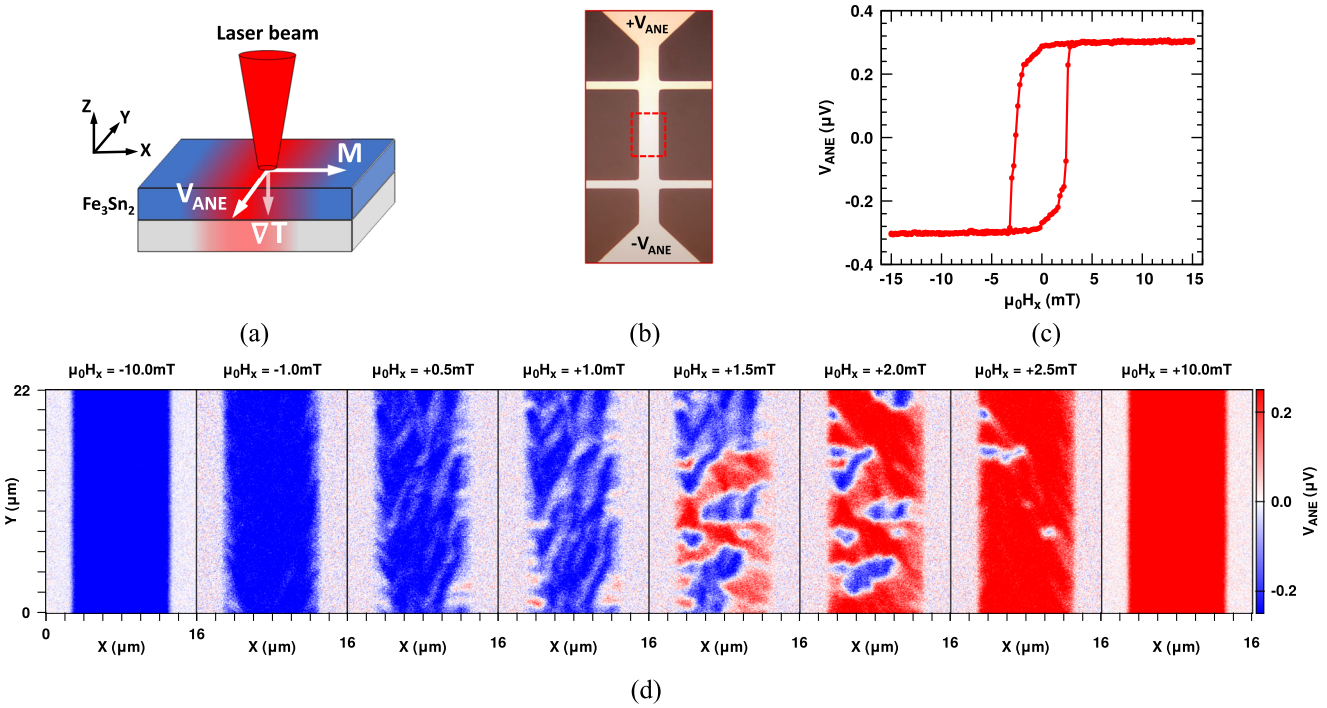

FIG. 4. Anomalous Nernst effect imaging. (a) Schematics of thermal gradient microscopy. The laser beam is scanned over the sample surface, and the induced local ANE voltage reflects the local magnetic properties. (b) Microscope image of a typical device [the dashed rectangle corresponds to the area imaged in (d)]. (c) ANE hysteresis loop of a 20 nm Fe_3Sn_2 film. (d) Magnetization reversal of a 20 nm film through multidomain state imaged by ANE at a series of magnetic fields $\mu_0 H_x$.

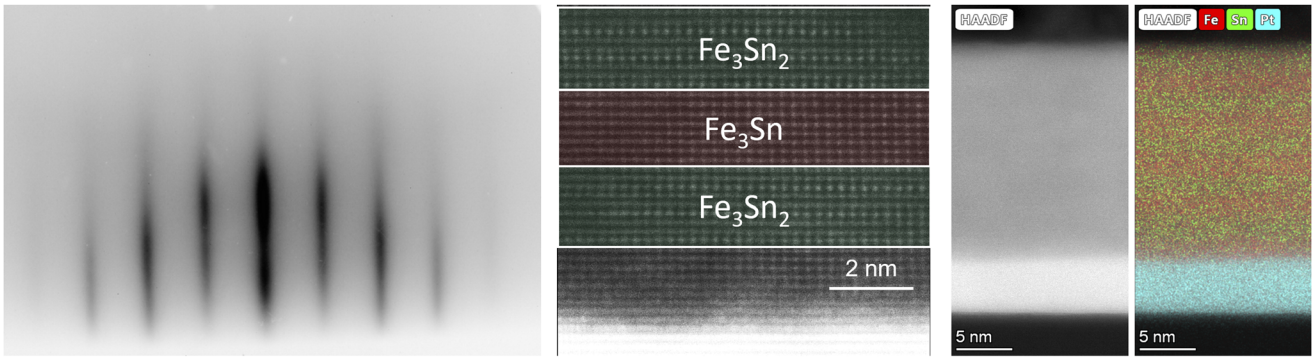

FIG. 5. $[Fe_3Sn_2/Fe_3Sn]_5$ superlattice. (a) RHEED pattern of $[Fe_3Sn_2/Fe_3Sn]_5$ superlattice. (b) TEM image of $[Fe_3Sn_2/Fe_3Sn]_5$ superlattice. (c) EDX of $[Fe_3Sn_2/Fe_3Sn]_5$ superlattice.

atomic layers of Fe_3Sn without any Sn_2 spacers. For a 2 nm Fe_3Sn_2 layer, we deposit two atomic layers of Fe_3Sn and one atomic layer of Sn_2 and repeat a total of three times. The RHEED pattern of a $[Fe_3Sn_2/Fe_3Sn]_5$ superlattice along the $[11\bar{2}0]$ direction of c-sapphire is shown in Fig. 5(a). The XRD data of the $[Fe_3Sn_2/Fe_3Sn]_5$ superlattice are shown in the supplementary material, Sec. 2.

Such control of the stacking sequence with atomic level precision is confirmed by the HAADF STEM image of the $[Fe_3Sn_2/Fe_3Sn]$ superlattice structure in Fig. 5(b). From the STEM image, an alternating sequence of 2 nm Fe_3Sn_2 (false colored in green) and 2 nm Fe_3Sn (false colored in red) can be observed with atomic resolution. Within 2 nm Fe_3Sn_2 layer, a repetitive stacking of two Fe_3Sn atomic layers and one Sn_2 atomic layer can be observed. In contrast, we can only see Fe_3Sn atomic layers in 2 nm Fe_3Sn layer. The STEM-EDX chemical map further reveals the repetition of the $[Fe_3Sn_2/Fe_3Sn]_5$ superlattice structure along the growth direction as shown in Fig. 5(c), where a 2 nm Fe_3Sn_2 layer has a stronger signal for the Sn element compared to a 2 nm Fe_3Sn layer.

We studied the magnetic properties of $[Fe_3Sn_2/Fe_3Sn]_5$ superlattice samples and compared them to 20 nm Fe_3Sn_2 samples (see the supplementary material, Sec. 6). The $[Fe_3Sn_2/Fe_3Sn]_5$ superlattice samples also have easy-plane anisotropy with square hysteresis loops, and very weak anisotropy within the sample plane, as shown by MOKE measurements. However, the longitudinal MOKE signal amplitude for the $[Fe_3Sn_2/Fe_3Sn]_5$ superlattice is slightly larger than 20 nm Fe_3Sn_2. The SQUID measurements show that the $[Fe_3Sn_2/Fe_3Sn]_5$ superlattice samples have larger out-of-plane saturation field (~1.7 T) and larger saturation magnetization (2.2 μ_B/Fe). This can be understood because Fe_3Sn has larger saturation magnetization and larger out-of-plane saturation field than Fe_3Sn_2.[26–28]

In conclusion, we report the atomic layer epitaxy growth of kagome ferromagnet Fe_3Sn_2 thin films on $Pt(111)/Al_2O_3(0001)$ at low temperatures. The high quality of epitaxial Fe_3Sn_2 films is confirmed by *in situ* RHEED, XRD, AFM, and TEM. Low temperature growth helps to generate a sharp interface between Fe_3Sn_2 and Pt layers, which has been observed by EDX. The magnetic properties are investigated by magneto-optical Kerr effect, SQUID magnetometry, and anomalous Nernst effect, confirming the easy-plane magnetic anisotropy of the thin films. Using ANE microscopy, we successfully resolve the local in-plane oriented micrometer size domains during magnetization reversal. Finally, we demonstrate the ability to control the sample structure at the atomic level by synthesizing $[Fe_3Sn_2/Fe_3Sn]_5$ superlattices and confirming their structure by TEM. These advances enable novel heterostructures for exploring the rich physics of kagome magnets.

See the supplementary material for additional AFM, XRD, EELS, MOKE, and SQUID data.

S.C., B.W., I.L., N.B., D.W.M., and R.K.K. acknowledge the support from DARPA (Grant No. D18AP00008). A.J.B. and R.K.K. acknowledge the support from AFOSR MURI 2D MAGIC (Grant No. FA9550-19-1-0390) and DOE (Grant No. DE-SC0016379). B.W. acknowledges the support from the Presidential Fellowship of the Ohio State University. This research was partially supported by the Center for Emergent Materials, an NSF MRSEC, under Award No. DMR-2011876. Electron microscopy experiments were supported by the Center for Electron Microscopy and Analysis at the Ohio State University.

AUTHOR DECLARATIONS

Conflict of Interest

The authors have no conflicts to disclose.

Author Contributions

Shuyu Cheng: Conceptualization (lead); Investigation (lead); Writing – original draft (lead). **Binbin Wang:** Investigation (lead); Writing – original draft (supporting). **Igor Lyalin:** Conceptualization (lead); Investigation (lead); Writing – original draft (lead). **Núria Bagués:** Investigation (supporting); Writing – original draft (supporting). **Alexander J. Bishop:** Investigation (supporting); Writing – original draft. **David W. McComb:** Supervision

(lead); Writing – original draft (lead). **Roland K. Kawakami:** Conceptualization (lead); Supervision (lead); Writing – original draft (lead).

DATA AVAILABILITY

The data that support the findings of this study are available from the corresponding author upon reasonable request.

REFERENCES

[1] L. Šmejkal, Y. Mokrousov, B. Yan, and A. H. MacDonald, "Topological antiferromagnetic spintronics," Nat. Phys. **14**, 242–251 (2018).

[2] H. Yang, Y. Sun, Y. Zhang, W.-J. Shi, S. S. P. Parkin, and B. Yan, "Topological Weyl semimetals in the chiral antiferromagnetic materials Mn_3Ge and Mn_3Sn," New J. Phys. **19**, 015008 (2017).

[3] K. Kuroda, T. Tomita, M.-T. Suzuki, C. Bareille, A. A. Nugroho, P. Goswami, M. Ochi, M. Ikhlas, M. Nakayama, S. Akebi, R. Noguchi, R. Ishii, N. Inami, K. Ono, H. Kumigashira, A. Varykhalov, T. Muro, T. Koretsune, R. Arita, S. Shin, T. Kondo, and S. Nakatsuji, "Evidence for magnetic Weyl fermions in a correlated metal," Nat. Mater. **16**, 1090–1095 (2017).

[4] L. Ye, M. Kang, J. Liu, F. von Cube, C. R. Wicker, T. Suzuki, C. Jozwiak, A. Bostwick, E. Rotenberg, D. C. Bell, L. Fu, R. Comin, and J. G. Checkelsky, "Massive Dirac fermions in a ferromagnetic kagome metal," Nature **555**, 638–642 (2018).

[5] M. Kang, L. Ye, S. Fang, J.-S. You, A. Levitan, M. Han, J. I. Facio, C. Jozwiak, A. Bostwick, E. Rotenberg, M. K. Chan, R. D. McDonald, D. Graf, K. Kaznatcheev, E. Vescovo, D. C. Bell, E. Kaxiras, J. van den Brink, M. Richter, M. Prasad Ghimire, J. G. Checkelsky, and R. Comin, "Dirac fermions and flat bands in the ideal kagome metal FeSn," Nat. Mater. **19**, 163–169 (2020).

[6] M. Kang, S. Fang, L. Ye, H. C. Po, J. Denlinger, C. Jozwiak, A. Bostwick, E. Rotenberg, E. Kaxiras, J. G. Checkelsky, and R. Comin, "Topological flat bands in frustrated kagome lattice CoSn," Nat. Commun. **11**, 4004 (2020).

[7] J.-X. Yin, S. S. Zhang, G. Chang, Q. Wang, S. S. Tsirkin, Z. Guguchia, B. Lian, H. Zhou, K. Jiang, I. Belopolski, N. Shumiya, D. Multer, M. Litskevich, T. A. Cochran, H. Lin, Z. Wang, T. Neupert, S. Jia, H. Lei, and M. Z. Hasan, "Negative flat band magnetism in a spin–orbit-coupled correlated kagome magnet," Nat. Phys. **15**, 443–448 (2019).

[8] T. Chen, T. Tomita, S. Minami, M. Fu, T. Koretsune, M. Kitatani, I. Muhammad, D. Nishio-Hamane, R. Ishii, F. Ishii, R. Arita, and S. Nakatsuji, "Anomalous transport due to Weyl fermions in the chiral antiferromagnets Mn_3X, X = Sn, Ge," Nat. Commun. **12**, 572 (2021).

[9] L. A. Fenner, A. A. Dee, and A. S. Wills, "Non-collinearity and spin frustration in the itinerant kagome ferromagnet Fe_3Sn_2," J. Phys.: Condens. Matter **21**, 452202 (2009).

[10] S. Nakatsuji, N. Kiyohara, and T. Higo, "Large anomalous Hall effect in a non-collinear antiferromagnet at room temperature," Nature **527**, 212–215 (2015).

[11] T. Higo, H. Man, D. B. Gopman, L. Wu, T. Koretsune, O. M. J. van 't Erve, Y. P. Kabanov, D. Rees, Y. Li, M.-T. Suzuki, S. Patankar, M. Ikhlas, C. L. Chien, R. Arita, R. D. Shull, J. Orenstein, and S. Nakatsuji, "Large magneto-optical Kerr effect and imaging of magnetic octupole domains in an antiferromagnetic metal," Nat. Photonics **12**, 73–78 (2018).

[12] Z. Hou, W. Ren, B. Ding, G. Xu, Y. Wang, B. Yang, Q. Zhang, Y. Zhang, E. Liu, F. Xu, W. Wang, G. Wu, X. Zhang, B. Shen, and Z. Zhang, "Observation of various and spontaneous magnetic skyrmionic bubbles at room temperature in a frustrated kagome magnet with uniaxial magnetic anisotropy," Adv. Mater. **29**, 1701144 (2017).

[13] Z. Hou, Q. Zhang, G. Xu, S. Zhang, C. Gong, B. Ding, H. Li, F. Xu, Y. Yao, E. Liu, G. Wu, X.-x. Zhang, and W. Wang, "Manipulating the topology of nanoscale skyrmion bubbles by spatially geometric confinement," ACS Nano **13**, 922–929 (2019).

[14] T. Kida, L. A. Fenner, A. A. Dee, I. Terasaki, M. Hagiwara, and A. S. Wills, "The giant anomalous Hall effect in the ferromagnet Fe_3Sn_2—A frustrated kagome metal," J. Phys.: Condens. Matter **23**, 112205 (2011).

[15] A. K. Nayak, J. E. Fischer, Y. Sun, B. Yan, J. Karel, A. C. Komarek, C. Shekhar, N. Kumar, W. Schnelle, J. Kübler, C. Felser, and S. S. P. Parkin, "Large anomalous Hall effect driven by a nonvanishing Berry curvature in the noncolinear antiferromagnet Mn_3Ge," Sci. Adv. **2**, e1501870 (2016).

[16] A. Markou, J. M. Taylor, A. Kalache, P. Werner, S. S. P. Parkin, and C. Felser, "Noncollinear antiferromagnetic Mn_3Sn films," Phys. Rev. Mater. **2**, 051001 (2018).

[17] H. Inoue, M. Han, L. Ye, T. Suzuki, and J. G. Checkelsky, "Molecular beam epitaxy growth of antiferromagnetic Kagome metal FeSn," Appl. Phys. Lett. **115**, 072403 (2019).

[18] J. M. Taylor, A. Markou, E. Lesne, P. K. Sivakumar, C. Luo, F. Radu, P. Werner, C. Felser, and S. S. P. Parkin, "Anomalous and topological Hall effects in epitaxial thin films of the noncollinear antiferromagnet Mn_3Sn," Phys. Rev. B **101**, 094404 (2020).

[19] D. Khadka, T. R. Thapaliya, S. Hurtado Parra, J. Wen, R. Need, J. M. Kikkawa, and S. X. Huang, "Anomalous Hall and Nernst effects in epitaxial films of topological kagome magnet Fe_3Sn_2," Phys. Rev. Mater. **4**, 084203 (2020).

[20] D. Hong, C. Liu, H.-W. Hsiao, D. Jin, J. E. Pearson, J.-M. Zuo, and A. Bhattacharya, "Molecular beam epitaxy of the magnetic kagome metal FeSn on $LaAlO_3$(111)," AIP Adv. **10**, 105017 (2020).

[21] H. Giefers and M. Nicol, "High pressure X-ray diffraction study of all Fe–Sn intermetallic compounds and one Fe–Sn solid solution," J. Alloys Compd. **422**, 132–144 (2006).

[22] B. Wang, P.-k. Wu, N. Bagués Salguero, Q. Zheng, J. Yan, M. Randeria, and D. W. McComb, "Stimulated nucleation of skyrmions in a centrosymmetric magnet," ACS Nano **15**, 13495–13503 (2021).

[23] M. Weiler, M. Althammer, F. D. Czeschka, H. Huebl, M. S. Wagner, M. Opel, I.-M. Imort, G. Reiss, A. Thomas, R. Gross, and S. T. B. Goennenwein, "Local charge and spin currents in magnetothermal landscapes," Phys. Rev. Lett. **108**, 106602 (2012).

[24] I. Gray, T. Moriyama, N. Sivadas, G. M. Stiehl, J. T. Heron, R. Need, B. J. Kirby, D. H. Low, K. C. Nowack, D. G. Schlom, D. C. Ralph, T. Ono, and G. D. Fuchs, "Spin Seebeck imaging of spin-torque switching in antiferromagnetic Pt/NiO heterostructures," Phys. Rev. X **9**, 041016 (2019).

[25] H. Reichlova, T. Janda, J. Godinho, A. Markou, D. Kriegner, R. Schlitz, J. Zelezny, Z. Soban, M. Bejarano, H. Schultheiss, P. Nemec, T. Jungwirth, C. Felser, J. Wunderlich, and S. T. B. Goennenwein, "Imaging and writing magnetic domains in the non-collinear antiferromagnet Mn_3Sn," Nat. Commun. **10**, 5459 (2019).

[26] B. C. Sales, B. Saparov, M. A. McGuire, D. J. Singh, and D. S. Parker, "Ferromagnetism of Fe_3Sn and alloys," Sci. Rep. **4**, 7024–7026 (2014).

[27] C. Echevarria-Bonet, N. Iglesias, J. S. Garitaonandia, D. Salazar, G. C. Hadjipanayis, and J. M. Barandiaran, "Structural and magnetic properties of hexagonal Fe_3Sn prepared by non-equilibrium techniques," J. Alloys Compd. **769**, 843–847 (2018).

[28] K. Fujiwara, Y. Kato, T. Seki, K. Nomura, K. Takanashi, Y. Motome, and A. Tsukazaki, "Tuning scalar spin chirality in ultrathin films of the kagome-lattice ferromagnet Fe_3Sn," Commun. Mater. **2**, 113 (2021).